Mon. Not. R. Astron. Soc. **000**, 1–?? (2014) Printed 30 October 2014 (MN LaTeX style file v2.2)

Kinematics of a globular cluster with an extended profile: NGC 5694. ⋆

M. Bellazzini[1]†, A. Mucciarelli[2], A. Sollima[1], M. Catelan[3,9], E. Dalessandro[2], M. Correnti[4], , V. D'Orazi[5,6], C. Cortés[7,9], P. Amigo[8,9]
[1] *INAF-Osservatorio Astronomico di Bologna, Via Ranzani 1, 40127, Bologna, Italy.*
[2] *Dip. di Astronomia - Univ. di Bologna, Via Ranzani 1, 40127, Bologna, Italy.*
[3] *Instituto de Astrofísica, Pontificia Universidad Católica de Chile, Av. Vicuna Mackenna 4860, 782-0436 Macul, Santiago, Chile*
[4] *Space Telescope Science Institute, 3700 San Martin Drive, Baltimore, MD 21218, USA*
[5] *Department of Physics and Astronomy, Macquarie University, Sydney, NSW 2109, Australia*
[6] *Monash Centre for Astrophysics, School of Mathematical Sciences, Monash University, Melbourne, VIC 3800, Australia*
[7] *Departamento de Física, Facultad de Ciencias Básicas, Universidad Metropolitana de Ciencias de la Educación,*
[8] *Departamento de Física y Astronomía, Universidad de Valparaíso, Av. Gran Bretaña 1111, Playa Ancha, Valparaíso, Chile Av. José Pedro Alessandri 774, 776-0197 Ñuñoa, Santiago, Chile*
[9] *Millennium Institute of Astrophysics, Santiago, Chile*

arXiv:1410.7929v1 [astro-ph.SR] 29 Oct 2014

Accepted for publication by MNRAS on October 29, 2014

ABSTRACT

We present a study of the kinematics of the remote globular cluster NGC 5694 based on GIRAFFE@VLT medium resolution spectra. A sample of 165 individual stars selected to lie on the Red Giant Branch in the cluster Color Magnitude Diagram was considered. Using radial velocity and metallicity from Calcium triplet, we were able to select 83 bona-fide cluster members. The addition of six previously known members leads to a total sample of 89 cluster giants with typical uncertainties $\leqslant 1.0$ km/s in their radial velocity estimates. The sample covers a wide range of projected distances from the cluster center, from $\sim 0.2'$ to $6.5' \simeq 23$ half-light radii (r_h). We find only very weak rotation, as typical of metal-poor globular clusters. The velocity dispersion gently declines from a central value of $\sigma = 6.1$ km/s to $\sigma \simeq 2.5$ km/s at $\sim 2' \simeq 7.1 r_h$, then it remainins flat out to the next (and last) measured point of the dispersion profile, at $\sim 4' \simeq 14.0 r_h$, at odds with the predictions of isotropic King models. We show that both isotropic single-mass non-collisional models and multi-mass anisotropic models can reproduce the observed surface brightness and velocity dispersion profiles.

Key words: (Galaxy:) globular clusters: individual: NGC 5694 – stars: abundances

1 INTRODUCTION

NGC 5694 is a bright ($M_V = -8.0$) and remote ($D = 35.5$ kpc) old and metal-poor Galactic Globular Cluster (GC), located in the Hydra constellation. First discovered by W. Herschel in 1784, it has been recognised as a GC by Lampland & Tombaugh (1932). Because of its distance and low apparent magnitude, the first photometric studies of giant stars in this cluster have been conducted only in relatively recent epoch (Harris 1975; Ortolani & Gratton 1990). After the first integrated spectroscopic studies (see, e.g., Harris & Hesser 1976) spectroscopy of individual Red Giant stars in NGC 5694 have been carried out by Geisler et al. (1995) and, more recently, by Lee et al. (2006). The latter derived the chemical composition for one bright giant of the cluster from a high-resolution spectrum and found an abundance pattern different from ordinary stars and clusters in the Galactic Halo, more similar to those displayed by stars in dwarf spheroidal galaxies. The accretion of globular clusters into the halo of giant galaxies during the disruption of their parent dwarf galaxy is now established to have occurred in the Milky Way (see, e.g., Bellazzini, Ferraro & Ibata 2003; Law & Majewski 2010; Carballo-Bello et al. 2014, and references therein) and in M31 (Perina et al. 2009; Mackey et al. 2010, 2013). Dense nuclei of stripped dwarf satellites can also appear as massive GCs at the present epoch (see

⋆ Based on data obtained at the Very Large Telescope under the program 089.D-0094.
† E-mail: michele.bellazzini@oabo.inaf.it

Bekki & Norris 2006; Bellazzini et al. 2008; Seth et al. 2014, for references and discussion). Chemical tagging is one of the main technique to identify otherwise ordinary GCs as accreted from a former, and now fully disrupted, Galactic satellite.

To follow-up the intriguing finding by Lee et al. (2006) we started a multi-instrument observational campaign that allowed us (a) to trace the surface brightness (SB) profile of the cluster down to $\mu_V \simeq 30.0$ mag/arcsec^2, finding that it extends smoothly much beyond the tidal radius of the best-fitting King (1966) model and that it cannot be adequately fit neither by a King (1966), Wilson (1975) nor Elson, Fall & Freeman (1987) model (Correnti et al. 2011, C11 hereafter), and (b) to perform accurate abundance analysis from high-resolution spectra for *six* cluster giants, fully confirming that the cluster has a chemical pattern different from the Galactic Halo, with nearly solar [α/Fe] ratio and anomalously low abundances of Y, Ba, La and Eu, at [Fe/H]$\simeq -2.0$ (Mucciarelli et al. 2013a, Mu13 hereafter).

Here we present a study of the kinematics of the cluster, based on a large sample of medium-resolution spectra of stars selected to lie on the Red Giant Branch (RGB) in the color magnitude diagram of the cluster. The plan of the paper is the following: in Sect. 2 we present our observations and we describe the data reduction. In Sect. 3 and 4 we describe how we derived our estimates of the radial velocity and metallicity, respectively, from the available spectra. In Sect. 5 we present our criteria to select cluster members and the analysis of the cluster kinematics, including estimates of the dynamical mass. Finally in Sect. 6 we briefly summarise and discuss the results of the analysis.

2 OBSERVATIONS

The data have been acquired with the multi-object facility FLAMES@VLT (Pasquini et al. 2000) in the combined MEDUSA+UVES mode, allowing the simultaneous allocation of 8 UVES high-resolution fibres and 132 MEDUSA mid-resolution fibres. For the UVES spectra, discussed in details in Mu13, we employed the 580 Red Arm set-up, with spectral resolution $R \sim$40000 and wavelength coverage $\sim$4800–6800 Å. The GIRAFFE targets have been observed with the HR21 setup, with a resolving power of $\sim$16000 and a spectral coverage between $\sim$8480–9000 Å . This grating was chosen because it includes the prominent Ca II triplet lines, which are ideal to measure radial velocities (RV) also in spectra of faint stars and to derive an estimate of their metallicity.

Two configurations of target stars have been used. A total of 4 exposures of 46 min each for each configuration has been secured in Service Mode during the period between April and July 2012. A small overlap between the two configurations (12 stars) has been secured in order to cross-check the stability of the RV when measured with different fibres.

The target selection has been performed with the B,V photometric catalog by C11 obtained by combining VIMOS@VLT and WFPC2@HST data. We selected stars along the RGB with V<20. Stars with close (within 2 arcsec) companion stars of comparable or brighter magnitude have been discarded, to avoid spurious contaminations in the fibre. About 15-20 fibres in each configuration have been dedicated to sample the sky background, because this spectral range is affected by prominent O_2 and OH sky emission lines. Fig. 1 shows the (V, B-V) colour-magnitude diagram of NGC 5694 with with GIRAFFE targets marked as red circles and the UVES ones as blue asterisks. The spatial distribution of the targets with respect to the cluster center is shown in Fig. 2; a circle with radius equal to the cluster tidal radius of the K66 model providing the best-fit to the SB profile of NGC 5694, as derived in C11, is also plotted, for reference.

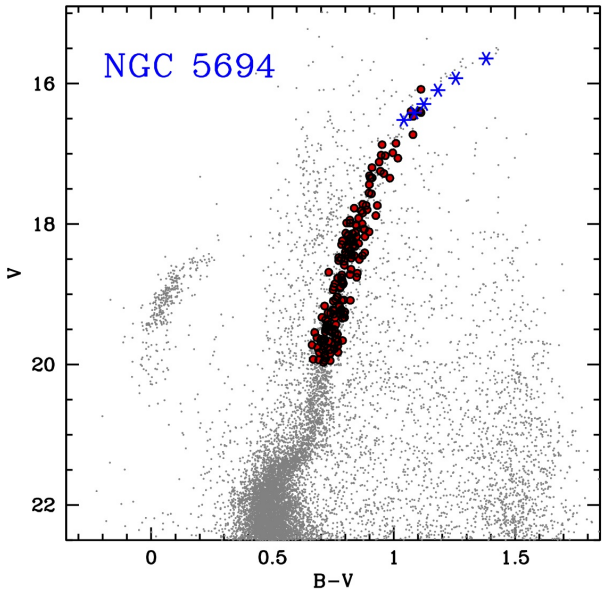

Figure 1. Color Magnitude Diagram of NGC5694 in the V, B-V plane from VIMOS@VLT and WFPC2@HST (grey small points). Red circles and blue asterisks are the GIRAFFE and UVES targets, respectively.

The data reduction has been performed using the last version of the ESO pipeline [1], including bias-subtraction, flat-fielding, wavelength calibration with a standard Th-Ar lamp and spectral extraction. The accuracy of the zero-point of the wavelength calibration has been checked by measuring the position of several sky emission lines and comparing them with their rest-frame position taken from the sky lines atlas by Osterbrock et al. (1996). For each star the average difference between the measured and reference line positions is always smaller than 0.02 Å, corresponding to less than one half of a pixel. These shifts turns out to be compatible with 0 within the quoted uncertainties. Hence, no relevant wavelengths shift is found.

Each individual stellar spectrum has been subtracted from the sky by using a master sky spectrum obtained as a median of the different sky spectra observed in that exposure. Then the proper heliocentric correction has been applied. Finally, individual spectra of the same target have been combined together. The typical SNR per pixel (measured at $\sim$8550 *Å*) is of $\sim$150 for the brightest targets (V$\sim$16) and of $\sim$10 for the faintest stars (V$\sim$20). Some tar-

[1] http://www.eso.org/sci/software/pipelines/

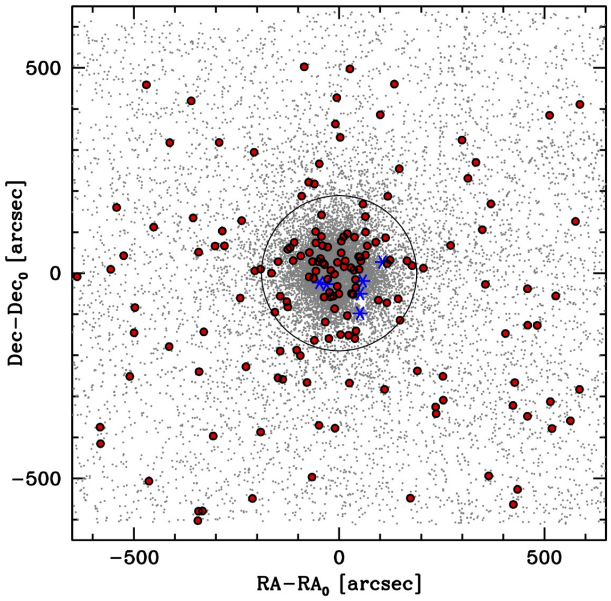

Figure 2. Spatial distribution of the FLAMES targets (same symbols of Fig. 1) with respect to the cluster center by Noyola & Gebhardt (2006). The black circle indicate the tidal radius of the K66 model providing the best-fit to the SB profile of NGC 5694 (from C11).

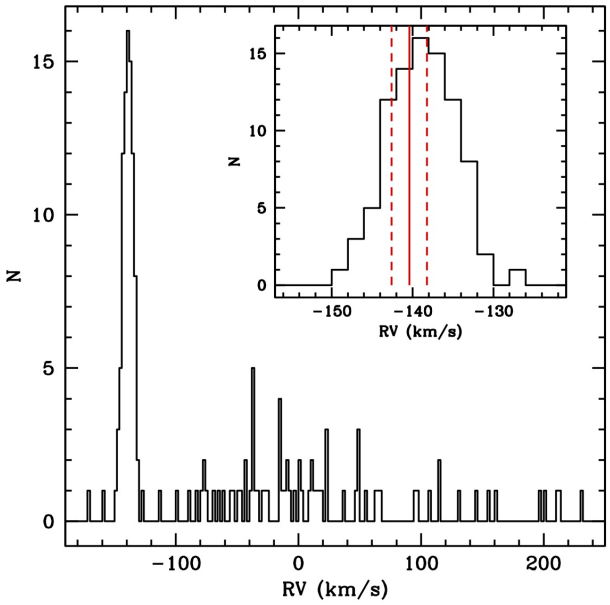

Figure 3. RV distribution of the stars of NGC 5694 observed with GIRAFFE. The inset panel shows a zoomed view of the region around the main peak of the distribution. The red solid line is the average RV obtained from the six UVES targets Mu13, while the two dashed lines indicate $\pm 1\sigma$ levels.

gets have been discarded because of the poor quality of their spectra or due to some residuals of the sky lines that can affect the correct RV measurement. Finally, the following analysis is based on 165 stars with reliable RV and metallicity estimates.

3 RADIAL VELOCITIES

RVs have been measured with the standard cross-correlation technique of the observed spectrum against a template of known RV, as implemented in the IRAF[2] task FXCOR. As template, we adopted a synthetic spectrum calculated with the code SYNTHE, adopting the entire atomic and molecular line-list by Kurucz and Castelli[3] and a ATLAS9 model atmosphere calculated with the metallicity of the cluster, [Fe/H]∼–2.0 dex and the typical atmospheric parameters of a giant star (T_{eff}= 4500 K, log(g)= 1.5). Uncertainties in the RV have been computed by FXCOR according to Tonry & Davis (1979), by taking into account the height and width of the cross-correlation function and the mean distance between its main peak and the nearest secondary peaks (Eq. 24 by Tonry & Davis 1979).

As an additional sanity check, the RVs of the 12 stars observed in both configurations have been measured individually. The two sets of RV agree very well each other, with a mean difference of $+0.5 \pm 0.5$ km/s, fully compatible with a null difference.

Fig. 3 shows the RV distribution of the entire sample of GIRAFFE targets. The distribution ranges from –171 km/s to +231 km/s, with a dominant peak around at ∼–140 km/s and corresponding to the cluster stars (the average RV derived from the 6 UVES targets is of -140.4±2.2 km/s). The inset panel shows a zoomed view of the region around the main peak of the RV distribution, with marked as a reference the average RV obtained from the UVES targets (red solid vertical line).

4 METALLICITY

4.1 Abundances from the Ca II triplet lines

Abundances for all the target stars have been obtained by using the strength of the Ca II triplet lines as a proxy of the metallicity. The lines of the Ca II triplet lines have been fitted with a Voigt profile, in order to reproduce the prominent pressure-broadened line wings, and then their equivalent widths (EWs) obtained by direct integration of the best-fit profile. The metallicities have been obtained by adopting the calibration by Carrera et al. (2007) and assuming V_{HB}= 18.5 mag (Harris 1996, 2010 edition).

Uncertainties in the measured EWs of the Ca II triplet lines have been estimated by employing Monte Carlo simulations. A synthetic spectrum has been re-sampled at the pixel-size of the GIRAFFE spectra (0.05 Å /pixel) and then Poissonian noise corresponding to four values of SNR (namely 10,50,100,150) has been injected in order to simulate the noise conditions of the observed spectra. For each value of SNR, 1000 synthetic spectra have been generated

[2] IRAF (Image Reduction and Analysis Facility) is distributed by the National Optical Astronomy Observatory, which is operated by the Association of Universities for Research in Astronomy, Inc., under cooperative agreement with the National Science Foundation.

[3] http://wwwuser.oat.ts.astro.it/castelli/odfnew.html

following this approach, the EWs of the Ca II triplet lines have been measured and then the metallicity estimated as done for the observed spectra. For each SNR, the uncertainty has been computed as 1σ of the derived [Fe/H] distribution; the abundance uncertainty is of 0.13 dex for SNR= 10 and 0.01 dex for SNR= 150. A relation that provides $\sigma_{[Fe/H]}$ as a function of SNR has been derived and used to estimate the uncertainty in [Fe/H] of all the targets interpolating at their value of the SNR. Additional sources of uncertainty are the error in V-V_{HB} (a variation of $\pm$0.05 mag translates in a variation in [Fe/H] of $\mp$0.01 dex) and the uncertainty in the EW_{CaT}–[Fe/H] linear fit (σ= 0.08 dex, as quoted by Carrera et al. 2007). The distribution of the [Fe/H] abundance ratios as derived from Ca II triplet lines is shown in Fig. 4 as an empty histogram.

4.2 Abundances from the Fe I lines

For 19 targets, the quality of the spectra (SNR>40) allows to determine the iron abundance directly from the measure of Fe I lines. We identify a ten of Fe I lines, unblended at the HR21 setup resolution and at the atmospheric parameters and metallicity of the targets (see Mu13, for details). EWs measurements have been performed by using the code DAOSPEC (Stetson & Pancino 2008), iteratively launched by means of the package 4DAO[4](Mucciarelli 2013b) that allows an analysis cascade of a large sample of stellar spectra and a visual inspection of the Gaussian fit obtained for all the investigated lines.

The iron abundance has been derived with the package GALA[5] (Mucciarelli et al. 2013c), by matching the measured and the theoretical EWs. Atmospheric parameters have been derived by using the B,V photometry by C11.

T_{eff} have been computed by means of the $(B-V)_0$–T_{eff} transformation by Alonso, Arribas & Martinez-Roger (1999) based on the Infrared Flux Method; the de-reddened color $(B-V)_0$ is obtained adopting a color excess E(B-V)= 0.099 mag (C11) and the extinction law by McCall (2004). Surface gravities have been computed with the Stefan-Boltzmann relation, assuming the photometric T_{eff}, the distance modulus of 17.75$\pm$0.10 mag (C11) and an evolutive mass of 0.75 $M_{\odot}$, according to an isochrone from the BaSTI dataset (Pietrinferni et al. 2004) with age of 12 Gyr, Z= 0.0003 and a solar-scaled chemical mixtures. The bolometric corrections are calculated according to Eq. (17) of Alonso, Arribas & Martinez-Roger (1999). Micro-turbulent velocities cannot be estimated from these spectra because of the small number of available lines and we adopted for all the targets the average value obtained by the UVES spectra, v_{turb}= 1.8 km/s.

The average iron abundance of these 19 stars is [Fe/H]=–2.04$\pm$0.02 dex, in reasonable agreement with the value derived by the UVES spectra, [Fe/H]=–1.98$\pm$0.03 dex (Mu13). Also, we highlight the good agreement between the abundances derived from Ca II triplet and from Fe I lines: the average difference of the iron abundances for the 19 stars in common is $[Fe/H]_{CaT} - [Fe/H]_{Fe} = +0.02 \pm 0.01$ dex (σ= 0.08 dex). Fig. 4 shows the distribution of the 19 stars as a grey histogram, while the inset panel shows the difference between [Fe/H] from Fe I lines and from Ca II lines.

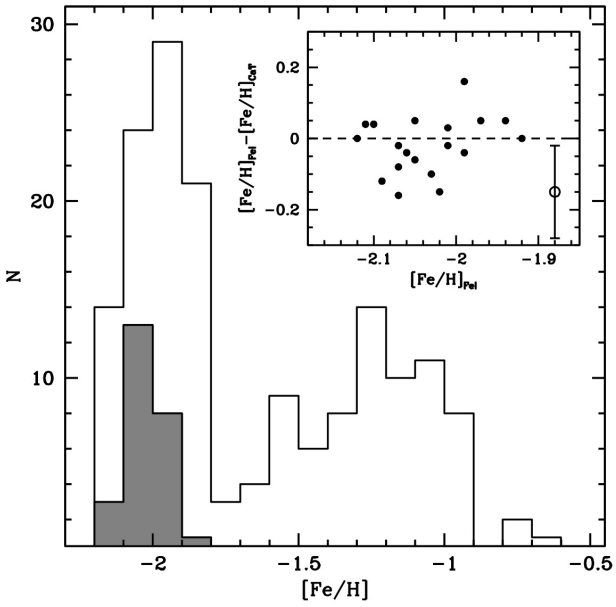

Figure 4. [Fe/H] distribution of the targets as obtained from the Ca II triplet lines (empty histogram) and from the direct measurement of Fe I lines (UVES+GIRAFFE, grey-shaded histogram). The inset panel show the difference between the iron content from Fe I lines and from Ca II triplet lines as a function of $[Fe/H]_{FeI}$ for 19 target stars observed with FLAMES. The typical uncertainty in the difference is shown as the error-bar of the empty circle in the lower-right corner of the inset.

We consider together the 25 stars for which a direct Fe abundance has been derived, 19 GIRAFFE and 6 UVES targets. The mean abundance, together with the intrinsic spread σ_{int} and their uncertainties, have been calculated with the maximum likelihood algorithm described in Mucciarelli et al. (2012). We obtain an average value of [Fe/H]=–2.01$\pm$0.02 dex (σ_{int}= 0.0$\pm$0.03 dex) that we recommended as the final value for the Fe abundance. In comparison, the same algorithm applied on the [Fe/H] derived from Ca II triplet lines of the 83 member stars provides [Fe/H]=–1.99$\pm$0.01 dex (σ_{int}= 0.0$\pm$0.02 dex).

5 KINEMATIC ANALYSIS

5.1 Membership

Fig. 5 compares the distribution of the RV as a function of [Fe/H] of our targets with that predicted by the Besancon Galactic Model (Robin et al. 2003) for a $1^{\circ} \times 1^{\circ}$ field in the direction of NGC 5694. In the right panel of Fig. 5 we plot only model stars with surface gravity in the range covered by cluster RGB stars (log(g)$<$ 3.0) and lying within a window in the CMD that encloses our targets ($0.6 < B-V < 1.4$ and $15.5 < V < 20.0$). Stars belonging to the cluster are very clearly identified in this plane, forming a tight and isolated concentration around $V_r \sim -140$ km/s and [Fe/H]~ -2.0. For this reason, we adopted the rectangular box plotted in both panels of the figure to select

[4] http://www.cosmic-lab.eu/4dao/4dao.php
[5] http://www.cosmic-lab.eu/gala/gala.php

Table 1. Main parameters for target stars observed with FLAMES: identification number, right ascension and declination, SNR per pixel, B and V magnitudes (C11), radial velocity, [Fe/H] from direct Fe I lines measurement and from Ca II triplet lines. Uncertainties in $[Fe/H]_{CaT}$ include both internal errors and the uncertainty in the calibration by Carrera et al. (2007). The entire table is available in the electronic version of the journal.

ID	RA (J2000)	Dec (J2000)	SNR (@8550Å)	B	V	RV (km/s)	$[Fe/H]_{Fe}$ (dex)	$[Fe/H]_{CaT}$ (dex)
65	219.8460466	-26.5338128	150	17.194	16.082	-33.15±0.52	—	–1.07±0.08
88	219.8965614	-26.5306057	140	17.498	16.391	-137.78±0.21	–1.92±0.11	–1.92±0.08
89	220.0596065	-26.6086914	80	17.467	16.396	-8.53±0.66	—	–1.39±0.08
94	219.8884807	-26.5485943	99	17.525	16.413	-138.75±0.21	–1.97±0.11	–2.02±0.08
99	219.9004115	-26.4470219	68	17.546	16.466	-10.71±0.58	—	–1.29±0.08

our sample of candidate cluster members. Target stars are selected as cluster members if they satisfy the conditions -160.0 km/s< V_r <-120.0 km/s and -2.3 <[Fe/H]< -1.7. It is reassuring to note that only one over 101 model stars falls within the selection box; given the difference in the sampled area, this corresponds to a probability $< 0.2\%$ to have a Galactic giant contaminating our sample. If also dwarf stars are considered (log g$\geqslant$ 3.0), only 1 model star over 5074 falls in the box. We can conclude that our selection criteria are robust and that all the selected stars can be considered as bona-fide cluster members[6].

According to these criteria, we selected 83 out 165 GIRAFFE targets. In the following we use the selected sample of 89 bona-fide members (83 GIRAFFE plus 6 UVES targets), located between $0.2'$ and $6.5'$ from the cluster center, to study the kinematics of the cluster. The mean RV value, computed with a maximum likelihood algorithm (ML hereafter; see Walker et al. 2006), is –139.2±0.4 km/s, in good agreement with previous estimates (Geisler et al. 1995; Dubath, Meylan & Mayor 1997; Lee et al. 2006).

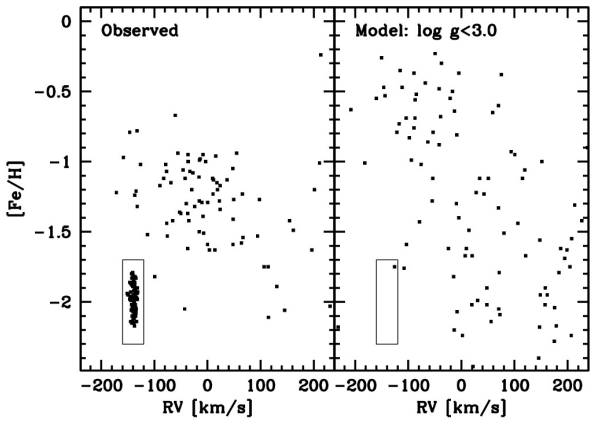

Figure 5. Comparison of our sample (left panel) with the predictions of the Besancon Galactic model (right panel) in the RV vs metallicity plane. The model stars are those predicted for a field of $1^\circ \times 1^\circ$ in the direction of the cluster. We included in this plot only stars in a color - magnitude window enclosing our targets ($0.6 < B-V < 1.4$ and $15.5 < V < 20.0$) and in the same range of surface gravity as cluster RGB stars (log g< 3.0). The thin rectangle is the box that we adopted to select our bona-fide cluster members.

5.2 Cluster rotation

We searched for rotation adopting the method and the notation described in Bellazzini et al. (2012). Basically, the sample is divided into two groups by a line passing from the cluster center, and the difference between the average RV of the two sub-samples, on each side of the dividing line, is computed. This step is repeated by varying the value of the position angle (PA) of the boundary line in steps of 10°.

The difference between the mean RV of the two subsamples as a function of PA is shown in Fig 6, together with the sine function that best fits the observed pattern. The best-fit sine function has a position angle of the rotation axis of 269° and an amplitude of the rotation curve of 0.7 km/s[7] According to Bellazzini et al. (2012) this very weak amplitude of the mean rotation is typical of clusters as metal-poor as (and with an Horizontal Branch - HB - morphology as blue as) NGC 5694. Since the rotation amplitude is significantly lower than the velocity dispersion over the whole radial range covered by our data (see below) it can be neglected in the following analysis.

5.3 Velocity dispersion

The projected velocity dispersion profile has been derived following the same procedure described in Bellazzini et al. (2008). The cluster area has been divided in 4 concentric annuli, in order to have in each radial bin a similar number of stars (∼20-24). In each radial bin the velocity dispersion σ_{RV} and the associated errors (ϵ_σ) have been computed with the ML method (Walker et al. 2006), keeping the systemic velocity fixed. An iterative 3σ clipping algorithm applied in each radial bin did not lead to the rejection of any additional star. The derived profile is reported in Table 2.

[6] It must be noted that [Fe/H] estimates from CaT for non-member stars are by definition not correct, since the $V - V_{HB}$ parameter is ill-defined for stars lying at any distance from the cluster. A variation of ±0.5 mag in the adopted distance modulus leads to a variation of $\mp$0.13 dex in the derived [Fe/H]. This behaviour is consistent with the different slopes in the [Fe/H]–RV plane found for the observed stars and the Besancon Galactic Model.

[7] A_{rot} is in fact the maximum difference between the mean velocity in the two considered halves of the cluster. This is two times the mean rotation amplitude in the considered radial range. Bellazzini et al. (2012) argue that in many cases A_{rot} is a reasonable proxy for the actual maximum amplitude.

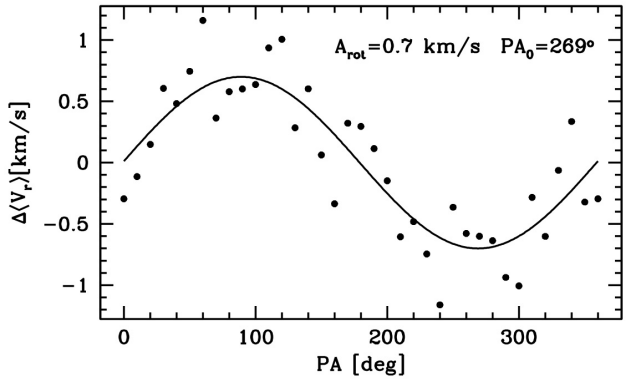

Figure 6. Rotation as derived from the FLAMES sample of NGC 5694. The difference between the average RV on each side of the cluster with respect to a line passing through the cluster center with a given position angle (PA) is shown as a function of the PA itself. The continuos line is the sine function that best fits the observed pattern, A_{rot} and PA_0 the best-fit amplitude and position angle (see Bellazzini et al. 2012).

In the following we will compare the observed velocity dispersion profile of NGC 5694 with different kind of theoretical models. A detailed assessment of the best model, as performed, e.g., in Ibata et al. (2011), is beyond the scope of the present analysis, and is also prevented by our lack of the full control of uncertainties in the composite SB profile by C11, that is required for that kind of analysis. On the other hand, our main purpose is to explore models that can provide a reasonable representation of both the SB and the velocity dispersion profile to get insight on the physical characteristics of this anomalous stellar system, within the boundaries of Newtonian dynamics.

5.3.1 Comparison with single-mass isotropic models

The upper panel of Fig. 7 shows the RV distribution as a function of the distance from the cluster center (assuming the coordinate of the center from Noyola & Gebhardt 2006) for the individual member stars. The lower panel of Fig. 7 shows the derived velocity dispersion profile, where the black dots are the values of σ_{RV} derived in each radial bin from our data. Our profile is complemented by the central value provided by Dubath, Meylan & Mayor (1997, σ_0= 6.1±1.3 km/s), obtained from integrated spectroscopy (empty point). The velocity dispersion gently declines from the center to $\sim 2' \simeq 7.1 r_h$[8], and then flattens out to $\sigma \simeq 2.5$ km/s in the two outermost bins. Note that the outermost point of our velocity dispersion profile lies at $\simeq 4'$, corresponding to more than $14 r_h$ from the center, and still is far away from the limits of the cluster, since in C11 we were able to trace the SB profile out to $R = 8.5' \simeq 30 r_h$.

In the lower panel of Fig. 7 we superimpose to the data the predictions of three models that fits the observed SB profile of the cluster (at least in the innermost regions, see C11 and Fig. 8). The models have been normalised to best fit the observed velocity dispersion profile. The first two models are the single-mass isotropic King (1966, K66 hereafter) and

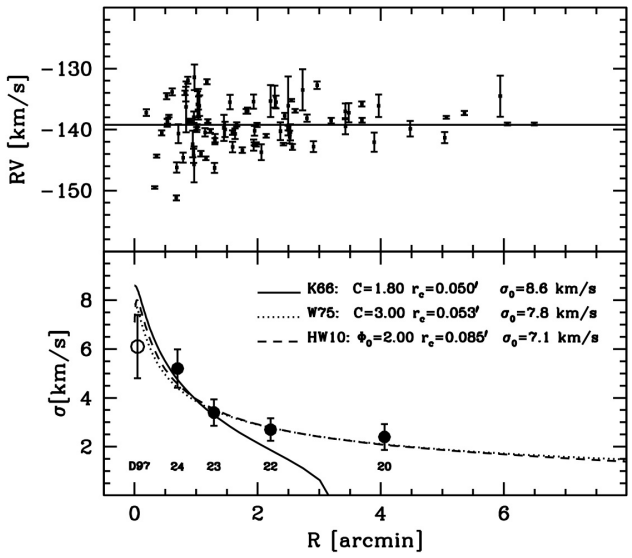

Figure 7. Upper panel: RV distribution of the individual member stars as a function of the distance from the cluster center. Solid horizontal line indicates the systemic RV of the cluster. Lower panel: velocity dispersion as a function of the distance from the cluster center from Table 2 (black circles). The open circle is the central velocity dispersion estimate from integrated spectroscopy by Dubath, Meylan & Mayor (1997). The number of stars per bin is also labelled. Theoretical models are over-imposed as comparison, namely by King (1966, solid curve), Wilson (1975, dotted curve) and Hjorth & Williams (2010, dashed curve). The parameters of the models adopted for the fit are also reported.

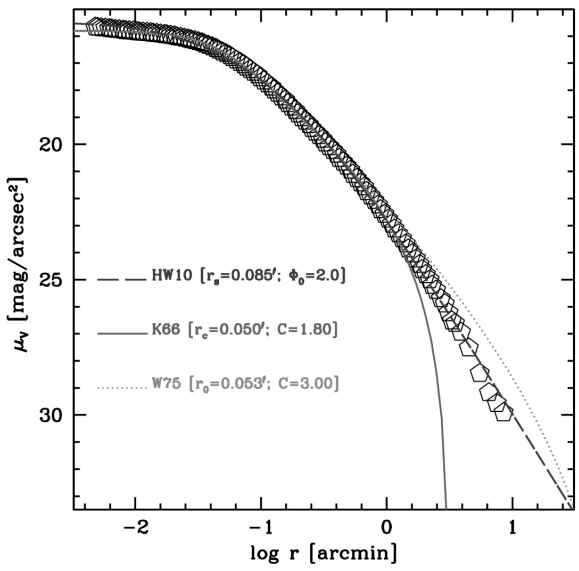

Figure 8. Surface brightness profile of NGC 5694 from C11. In addition to the single-mass isotropic King (1966) and Wilson (1975) models that best-fits the profile already shown in C11, we superimpose also a DARKexp model (Hjorth & Williams 2010) providing an acceptable fit over the whole extension of the observed profile.

[8] Where the observed half-light radius is $r_h = 0.28'$, from C11.

Table 2. Velocity dispersion profile.

R_{in} [arcmin]	R_{out} [arcmin]	$\langle R \rangle$ [arcmin]	σ_{RV} [km/s]	ϵ_σ [km/s]	N_{star}
0.0	1.0	0.70	5.2	0.78	24
1.0	1.8	1.29	3.4	0.54	23
1.8	2.6	2.21	2.7	0.46	22
2.6	7.8	4.06	2.4	0.53	20

Wilson (1975, W75) models that were proposed in C11. In addition to these we adopt also a *DARKexp* model (Hjorth & Williams 2010, HW10) that is shown, in Fig. 8, to provide a reasonable fit of the SB profile over the whole extension of the cluster, in particular in the outermost region of the profile where K66, W75 and Elson, Fall & Freeman (1987) models fail (see C11)[9]. DARKexp models are theoretically derived maximum entropy equilibrium states of self-gravitating collision-less systems (HW10). Williams, Barnes & Hjorth (2012) have shown that in many cases (including NGC 5694) they provide a better fit to the observed profiles of GCs, with respect to K66 models. The main difference between K66/W75 models and DARKexp models is in the assumed Distribution Function (DF; $f(E) \equiv \frac{dN}{d^3r\ d^3v}$). K66 and W75 models adopt a DF from the family of lowered Maxwellian distributions, which reproduces the trend toward an isothermal condition driven by collisions. DarkEXP models, instead, adopt a DF such that the corresponding energy distribution (N(E)=$f(E)\int r^2 v dv$) is a lowered Maxwellian distribution, with a proper treatment of the low-occupation-number regime (see Williams, Barnes & Hjorth 2012, for details and discussion).

The comparisons displayed in the lower panel of Fig. 7 clearly show the inadequacy of K66 models to describe the kinematics of NGC 5694. This is due to the tidal truncation that is built-in in K66 models: the SB profile is unable to fit the extended $\sim R^{-3}$ outer profile of the cluster and, consequently, it lacks sufficient mass in the outer regions to sustain a (nearly) flat dispersion profile beyond $R \sim 2'$. The lack of a tidal truncation may be related to the fact that the cluster is under-filling its Roche lobe by a significant amount (see C11 and Sect. 6, for further discussion). On the other hand both the W75 and DARKexp models, that have much more extended SB profiles, provide a fair representation of the cluster kinematics.

The central dispersion estimate by Dubath, Meylan & Mayor (1997) appears slightly low with respect to our innermost point and the extrapolation of all best-fitting models. It would be valuable to have an independent estimate of the dispersion in the innermost regions based on the velocities of individual stars, to obtain a robust validation of the estimate by Dubath, Meylan & Mayor (1997) from integrated spectroscopy. Moreover, it has to be recalled that in this comparison we considered only isotropic single-mass and non-collisional models. In the innermost regions of the cluster collisional processes can be important and mass-segregation, as well as anisotropy, is expected to contribute in shaping the overall line-of-sight velocity dispersion profile.

[9] It is interesting to note that also models with a larger number of free parameters than those considered here, like the Nuker or the core-Sersic models (see Graham et al. 2003), appear unable to provide a satisfactory fit to the entire SB profile of NGC 5694.

5.3.2 Comparison with multi-mass and anisotropic models

To explore the possible role of orbital anisotropy and mass segregation in the dynamics of NGC 5694 we compare, in Fig. 9, the observed SB and σ profiles of the clusters with the predictions of a model including radial anisotropy, two multi-mass models and one multi-mass anisotropic model.

The continuos lines in both panels of Fig. 9 correspond to a single-mass King-Michie (K-M Michie 1963) model with the maximum degree of radial anisotropy that still ensures stability (see Ibata et al. 2011, for a thorough discussion of this family of models). In these models, orbits are isotropic in the center and becomes radially biased at a characteristic radius r_a. A rough criterion for stability is represented by the so-called Fridman-Polyachenko-Shukhman parameter $\xi = 2T_r/T_t$ (Friedman & Polyachenko 1984), where T_r and T_t are the radial and tangential component of the kinetic energy tensor: a fully isotropic model have $\xi = 1$, while models with $\xi > 1.5$ undergo bar instability on timescales of few tens of dynamical times (Nipoti et al. 2002)[10]. The maximum degree of radial anisotropy of the considered K-M model ($r_a = 0.8\ r_h$; $\xi = 1.5$) is required to obtain a reasonable reproduction of the extended outer branch of the SB profile. The velocity dispersion profile provides a good description of the nearly-flat branch of the observed profile but it fails to fit the central point by more than six times the error on the central dispersion by Dubath, Meylan & Mayor (1997). It is interesting to note that excluding the central point to the best-fitting of the velocity normalisation leads to a nearly perfect fit to the profile, for $r > 0.5'$, but, in this case, the predicted value of the central dispersion is as high as 14.0 km/s.

In real clusters formed by stars with a mass spectrum and where the effects of collisions in the cluster center are non negligible, the density and velocity dispersion profiles are different for stars of different mass. Broadly speaking, massive stars tend to transfer kinetic energy to less massive stars thus becoming kinematically cooler and sinking in the innermost region of the cluster on less energetic orbits. The amount of kinetic energy transferred by a given star is a function of the contrast between its mass and the average mass of cluster stars, therefore depending on the Mass Function (MF). The three King multi-mass models shown in Fig. 9 as dotted, dashed and dot-dashed lines have been computed following Gunn & Griffin (1979, G79 hereafter) assuming 8 mass bins (all covering equal-mass intervals at different ranges) between 0.1 and 0.8 $M_\odot$ populated according to different assumption on the MF and degree of radial anisotropy: the dotted lines correspond to an isotropic model with a single power law MF (in the form

[10] The generally adopted parametrisation of orbital anisotropy through the $\beta = 1 - (v_t^2/v_r^2)$, where v_t and v_r are the tangential and radial components of the velocity, respectively, is not particularly informative for K-M models, since, by construction, they have $\beta = 0.0$ at their center and $\beta = 1.0$ in their outermost region, the shape of the distribution of β being characterised by the anisotropy radius r_a (see Ibata et al. 2011, and references therein).

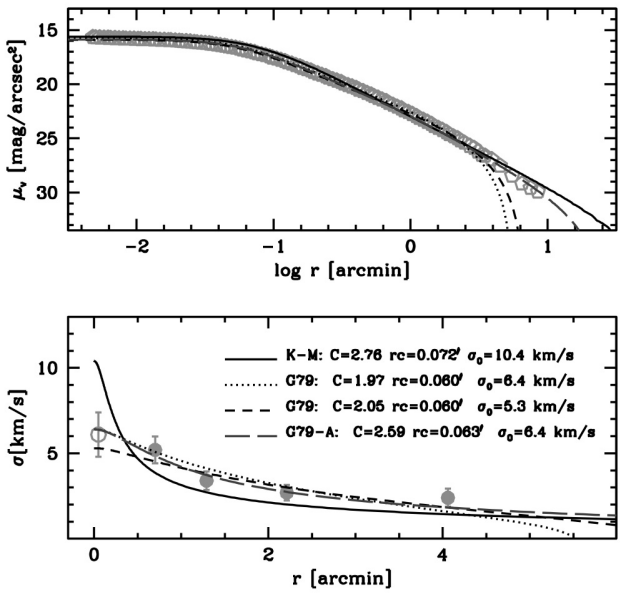

Figure 9. The surface brightness profile (upper panel) and the velocity dispersion profile (lower panel) of NGC 5694 are compared with a single-mass King-Michie model with radial anisotropy ($2T_r/T_t = 1.525$; continuous line), and with the predictions for the distribution of star in the largest mass bin (approximately corresponding to cluster giants) of two multi-mass King models computed following G79. The dotted lines correspond to a model with a single power law MF with index $x = -1$; the short-dashed lines correspond to a model with Kroupa (2001) MF. Finally, the long-dashed dark grey lines correspond to a multi-mass model with Kroupa (2001) MF and radial anisotropy. All the models have been normalised to best fit the observed velocity dispersion profile.

$Ndm \propto m^x$), with index $x = -1$, the short-dashed lines correspond to an isotropic model with a Kroupa (2001) MF and the long-dashed lines correspond to a radially anisotropic model ($r_a = 0.74\ r_h$) with a Kroupa (2001) MF. Dark remnants have been added to the original MF following the prescriptions by Sollima, Bellazzini & Lee (2012). Since our SB profile, and especially the velocity dispersion profile, are mainly based on giant stars we derived the best-fit by comparing them with the predictions for the most massive mass bin. While both the isotropic multi-mass models fails to reproduce the outer branch of the SB profile, they provide a good fit to the dispersion profile over the whole radial range. An even better fit is provided by the anisotropic model (with $r_a = 0.75\ r_h$; $\xi = 1.31$) which well reproduce the shape of both the SB and the velocity dispersion profile along their entire extent.

A gentler decline of the velocity dipersion curve with respect to isotropic K66 models is also predicted in the framework of the MOdified Newtonian Dynamics (Milgrom 1983). However in this case one would expect a convex shape of the velocity dispersion profile in contrast with our data, unless a high degree of radial anisotropy is present (i.e., higher than that assumed here for King-Michie models in Newtonian dynamics, see Sollima & Nipoti 2010). In general, given the good fit provided by darkEXP and multi-mass anisotropic models described above, we conclude that there is no need to invoke a modification of the Newtonian gravity to explain the observed structure and kinematics of this cluster.

5.3.3 Dynamical mass estimates

It is interesting to note that the masses of the three best-fitting isotropic single-mass models are fully consistent. For the K66 model we obtain $M_{K66} = 2.5{\times}10^5\ M_\odot$, for the W75 model $M_{W75} = 2.6 \times 10^5\ M_\odot$, and for the DARKexp model $M_{HW10} = 2.5 \times 10^5\ M_\odot$, corresponding to $\frac{M}{L_V} \simeq 1.8$. These values are in excellent agreement with the only previous dynamical mass estimate that can be found in the literature, i.e., $M = 2.5 \times 10^5\ M_\odot$ by Pryor & Meylan (1993), based on the central velocity dispersion from a preliminary analysis of the data of Dubath, Meylan & Mayor (1997). The agreement is good also with the non-dynamical estimates by McLaughlin & van der Marel (2005), who found $M = 2.1 \times 10^5\ M_\odot$ for both K66 and W75 models, adopting $M/L_V = 1.9$ and a total V luminosity lower than that estimated by C11 and used here ($M_V = -7.8$ instead of $M_V = -8.0$).

On the other hand, anisotropic and multi-mass models suggest a slightly larger mass, due to the fact that these models have a significant fraction of their kinetic energy in motions that are not accessible to a sampling of line-of-sight velocities of giants. The single-mass K-M anisotropic model gives $M_{KM} = 2.8 \times 10^5\ M_\odot$, the isotropic multi-mass models give $M_{G79} = 3.4{\times}10^5\ M_\odot$ and $M_{G79} = 3.6{\times}10^5\ M_\odot$ for the power-law MF with $x = -1$ and the Kroupa (2002) MF, respectively, and the anisotropic multi-mass model gives $M_{G79-A} = 4.9{\times}10^5\ M_\odot$. Using the anisotropy-independent estimator of the mass enclosed within the half light radius by Wolf et al. (2010), integrating over the observed SB profile and interpolating the dispersion profile with a spline, we obtain $M_{W,1/2} = 1.5{\times}10^5\ M_\odot$. Since in a star cluster the mass should approximately follow light (modulo the mass segregation) the total mass should be $M_{W,Tot} \sim 3.0 \times 10^5\ M_\odot$, also in reasonable agreement with the model-dependent estimates.

6 SUMMARY AND CONCLUSIONS

We obtained RV and [Fe/H] estimates from medium-resolution GIRAFFE spectra for 165 stars selected to lie on the RGB of the remote globular cluster NGC 5694. Using both RV and [Fe/H] we selected a sample of 89 bona-fide cluster members, 83 from the GIRAFFE sample and six from the UVES sample presented in Mu13. Based on these data we derived a mean cluster metallicity of [Fe/H]$= -2.01 \pm 0.02$, an intrinsic metallicity dispersion of $\sigma_{int} = 0.00 \pm 0.02$ dex and a systemic radial velocity of $V_{sys} = -139.2 \pm 0.4$ km/s.

The cluster kinematics is characterised by a very weak systemic rotation, fully consistent with the *rotation - metallicity* and *rotation - HB morphology* relations derived by Bellazzini et al. (2012). The velocity dispersion profile flattens out at large radii. This is incompatible with isotropic single-mass K66 models but is reasonably reproduced by both W75 and DARKexp models. However, W75 models provide an unsatisfactory fit to the the cluster SB profile, that, on the other hand is well reproduced by DARKexp models over

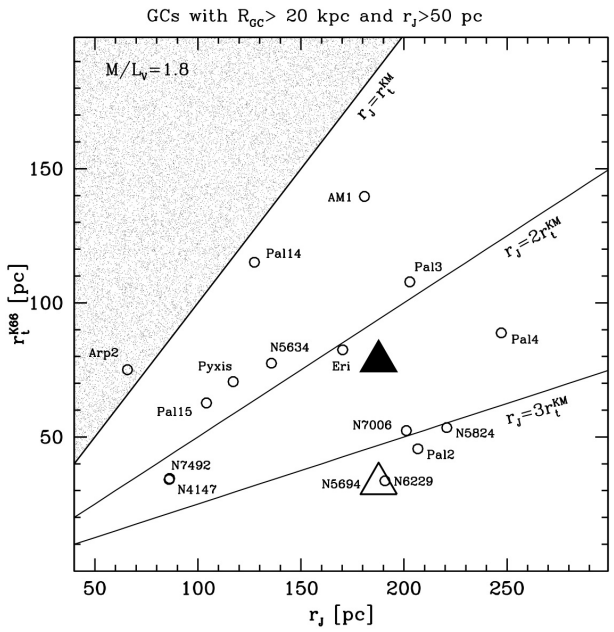

Figure 10. Jacoby radii versus tidal radii of the best-fitting K66 model for Galactic GCs more distant than 20 kpc from the Galactic center and having Jacoby radius larger than 50 pc (the latter selection has been introduced to make the plot as easy to read as possible; NGC 2419 is not included in the plot since it has a Jacobi radius much larger than all the other clusters,r_J = 604.4 pc). Lines at fixed r_J/r_t^{KM} ratio are also plotted for reference. NGC 5694 is plotted as an empty triangle when the K66 tidal radius is adopted, and as a filled triangle when the radius of the outermost point of our SB profile is adopted instead. The shaded area correspond to the region of over-filling clusters.

its whole extent. While anisotropic single-mass K-M models and multi-mass isotropic King models seem unable to provide an overall good representation of the structure and kinematics of the cluster, we showed that this result can be attained with multi-mass models including anisotropy.

Different models / mass estimators consistently converge on a mass between $M \simeq 2.5 \times 10^5\ M_\odot$, and $M \simeq 4.9 \times 10^5\ M_\odot$ corresponding to $\frac{M}{L_V} \simeq 1.8 - 3.5$ quite typical for GCs (Pryor & Meylan 1993; Sollima, Bellazzini & Lee 2012). The two models providing the best representation of both the SB and the σ profiles lie at the extremes of this range, the DARKexp isotropic non-collisional model at the lower end and the multi-mass anisotropic model (G79-A) at the upper end. The anisotropy-independent mass estimator by Wolf et al. (2010) is in better agreement with the DARKexp model, thus favouring mass (and mass-to-light) values toward the lower end. Low values of the mass-to-light ratio ($M/L_V \simeq 1.8$) are also in agreement with the predictions of population synthesis models, as derived by McLaughlin & van der Marel (2005). We do not report the uncertainties on the individual mass estimates (due to the errors in the input parameters, like, e.g., distance, radii, etc.) since they are significantly smaller than the the factor of ~ 2 systematic uncertainty that is associated to the choice of a given model (DARKexp or G79-A, in particular).

As noted in C11 and clearly illustrated in Fig. 10 (produced with the same assumptions as C11, adopting $M/L_V =$ 1.8, and taking tidal radii, total luminosities and Galactocentric distances from Harris 1996, 2010 edition) NGC 5694 is largely under-filling its Roche lobe, having a ratio between Jacoby radius and tidal radius $r_J/r_t^{KM} > 2.0$, independently on the actual assumption on the limiting radius (i.e., the tidal radius of the best-fitting K66 model or the outermost point of the observed profile). This holds also if the criterion by Baumgardt et al. (2010), based on the ratio between half-light radius and Jacoby radius ($r_h/r_J < 0.05$), is adopted: NGC 5694 has $r_h/r_J < 0.015$. These authors find that tidally under-filling clusters form a distinct family (compact clusters) with respect to tidally filling ones and concluded that they were likely born compact. The smooth nature of both the SB and the velocity dispersion profiles of NGC 5694 suggest that indeed it may be tidally undisturbed and may represent the typical status of a compact globular cluster evolved in isolation. This condition would also favour the permanence of an original radial anisotropic bias in the velocity distribution of cluster stars.

In this context, it is interesting to note that (a) virtually all the clusters shown in Fig. 10 and having $r_J/r_t^{KM} > 2.0$ display SB excesses in their outer regions, with respect to K66 models (see, e.g. Sohn et al. 2003; Jordi & Grebel 2010), and, in particular (b) many of the brightest among these clusters ($M_V < -7.5$) display smooth power-law profiles incompatible with K66 models in their outskirts, similar to NGC 5694 (see, e.g., Jordi & Grebel 2010; Sanna et al. 2012, 2014, for NGC 7006, NGC 6229, and NGC 5824, respectively) [11]. Deeper and more thorough analyses of the structure and kinematics of these clusters, extending into their low SB outskirts, seems timely. The study of a sample of distant *compact* clusters (in the sense defined by Baumgardt et al. 2010) may provide precious insight on the initial conditions of GCs whose evolution should be only weakly influenced by the interaction with the Milky Way.

ACKNOWLEDGMENTS

We are grateful to an anonymous referee for useful comments and suggestions. M.B. and A.S. acknowledges the financial support from PRIN MIUR, project: *The Chemical and Dynamical Evolution of the Milky Way and Local Group Galaxies*, prot. 2010LY5N2T, (PI F. Matteucci). Support for M.C., P.A., and C.C. is provided by the Ministry for the Economy, Development, and Tourism's Programa Iniciativa Científica Milenio through grant IC 120009, awarded to the Millennium Institute of Astrophysics (MAS). M.C. also acknowledges support by Proyecto Basal PFB-06/2007 and by FONDECYT grant #1141141.

REFERENCES

Alonso, A., Arribas, S., & Martinez-Roger, C., 1999, A&As, 140, 261

[11] NGC 2419 is well fitted by an anisotropic King-Michie model (see Ibata et al. 2011); Palomar 2 does not appear to have an anomalous profile, but the analysis may suffer from the impact of an high (and varying) interstellar extinction (Harris et al. 1997).

Baumgardt, H., Parmentier, G., Gieles, M., Vesperini, E., 2010, MNRAS, 401, 1832
Bellazzini, M., Ferraro, F.R., Ibata, R.A., 2004, AJ, 125, 188
Bellazzini, M., Ibata, R. A., Chapman, S. C., Mackey, A. D., Monaco, L., Irwin, M. J., Martin, N. F., Lewis, G. F. & Dalessandro, E., 2008, AJ, 136, 1147
Bellazzini, M., Bragaglia, A., Carretta, E., Gratton, R. G., Lucatello, S., Catanzaro, G., & Leone, F., 2012, A&A, 538, A18
Bekki, K., Norris, J.E., 2006, ApJ, 637, L109
Brown, J. A., Wallerstein, G., & Zucker, D., 1997, AH, 114, 180
Carballo-Bello, J.A., Sollima, A., Martinez-Delgado, D., et al., 2014, MNRAS, in press (arXiv:1409.7390)
Carrera, R., Gallart, C., Pancino, E., & Zinn, R., 2007, AJ, 135, 836
Carretta, E., Bragaglia, A., Gratton, R.G., et al., 2010, A&A, 52, 95
Carretta, E., Bragaglia, A., Gratton, R.G., D'orazi, V.D., Lucatello, S., Sollima, A., 2014, A&A, 561, A87
Correnti, M., Bellazzini, M., Dalessandro, E., Mucciarelli, A., Monaco, L., & Catelan, M., 2011, MNRAS, 417, 2411 (C11)
Da Costa, G.S., Held, E.V., Saviane, I., 2014, MNRAS, 438, 3507
Dubath, P., Meylan, G., & Mayor, M., 1997, A&A, 324, 505
Elson, R.A.W., Fall, S.M., Freema, K.C., 1987, ApJ, 323, 54
Ibata R., Sollima, A., Nipoti, C., Bellazzini, M., Chapman, S.C., Dalessandro, E., 2011, ApJ, 738, 186
Fridman, A.M., Polyachenko, V.L., 1984, Physics of Gravitating Systems. II. Nonlinear Collective Processes: Nonlinear Waves, Solitons, Collisionless Shocks, Turbulence (New York: Springer)
Geisler, D., Piatti, A. E., Claria, J. J., & Minniti, D., 1995, AJ, 109, 605
Graham, A.W., Erwin, P., Trujillo, I., Asensio Ramos, A., 2003, AJ, 125, 2951
Gratton, R., Carretta, E., Bragaglia, A., 2012, A&AR, 20, 50
Gunn, J.E., Griffin, R.F., 1979, AJ, 84, 752
Jordi, K., Grebel, E.K., 2010, A&A, 522, A71
Harris, W.E., 1975, ApJS, 29, 397
Harris, W.E., Hesser, J.E., 1976, PASP, 88, 377
Harris, W.E., Durrell. P.R., Petitpas, G.R., Webb, T.M., Woodworth, S.C., 1997, AJ, 114, 1043
Harris, W. E., 1996, AJ, 112, 1487
Hjorth, J., & Williams, L. L. R., 2010, ApJ, 722, 851
King, I. R., 1966, AJ, 71, 64
Kroupa, P., 2001, MNRAS, 322, 231
Küpper, A.H.W., Kroupa, P., Baumgardt, H., Heggie, D.C., 2010, MNRAS, 407, 2241
Lampland, C.O., Tombaugh, C.W., 1932, AN, 246, 171
Law, D.R., majewski, S.R., 2010, ApJ, 718, 1128
Lee, J.-W., Lopez-Morales, M., & Carney, B. W., 2006, ApJ, 646L, 119
Lupton, R., 1993, in Statistics in Theory and Practice (Princeton, NJ: Princeton Univ. Press)
Mackey, A.D., Huxor, A.P., Ferguson, A.M.N., et al., 2010, ApJ, 717, L11
Mackey, A.D., Huxor, A.P., Ferguson, A.M.N., et al., 2013, MNRAS, 429, 281
McCall, M. L., 2004, AJ, 128, 2144
McLaughlin, D. E., & van der Marel, R. P., 2005, ApJS, 161, 304
McWilliam, A., Wallerstein, G., Mottini, M., 2013, ApJ, 778, 149
Michie, R.W.,1963, MNRAS, 125, 127
Milgrom, M., 1983, ApJ, 270, 365
Monaco, L., Bellazzini, M., Bonifacio, P., Ferraro, F.R., Marconi, G., Pancino, E., Sbordone, L., Zaggia, S., 2004, A&A, 441, 141
Mucciarelli, A., Bellazzini, M., Ibata, R., Merle, T., Chapman, S. C., Dalessandro, E., & Sollima, A., 2012, MNRAS, 426, 2889
Mucciarelli, A., Bellazzini, M., Catelan, M., Dalessandro, E., Amigo, P., Correnti, M., Cortés, C.& D'Orazi, V, 2013a, MNRAS, 435, 36 (M13)
Mucciarelli, A., 2013b, arXiv1311.1403
Mucciarelli, A., Pancino, E., Lovisi, L., Ferraro, F. R., & Lapenna, E., 2013c, ApJ, 766, 78 67
Noyola, E., & Gebhardt, K., 2006, AJ, 132, 447
Ortolani, S., Gratton, R., 1990, A&AS, 82, 71
Osterbrock, D. E., Fulbright, J. P., Martel, A. R., Keane, M. J., Trager, S. C., & Basri, G., 1996, PASP, 108, 277
Pasquini, L., et al., 2000, SPIE, 4008, 129
Perina, S., Federici, L., Bellazzini, M., Cacciari, C., Fusi Pecci, F., Galleti, S., 2009, A&A, 507, 1375
Pietrinferni, A., Cassisi, S., Salaris, M. & Castelli, F., 2004, ApJ, 612, 168
Pryor, C., Meylan, G., 1993, in Structure and Dynamics of Globular Clusters, ed. S. G. Djorgovski & G. Meylan (San Francisco, CA: ASP), ASP Conf. Ser. 50, 357
Robin, A. C., Reulé, C., Derriere, S. & Picaud, S., 2003, A&A, 409, 523
Stetson, P. & Pancino, E., 2008, PASP, 120, 1332
Tonry, J., & Davis, M., 1979, 84, 1511
Trager, S. C., King, I. R., & Djorgovski, S., 1995, AJ, 109, 218
Sanna, N., Dalessandro, E., Lanzoni, B., Ferraro, F.R., Beccari, G., Rood, R.T., 2012, MNRAS, 422, 1171
Sanna, N., Dalessandro, E., Ferraro, F.R., Lanzoni, B., Miocchi, P., O'Connell, R.W., 2014, ApJ, 780, 90
Seth, A.C., van den Bosch, R., Mieske, S., et al., 2014, Nature, 513, 398
Sohn, Y.-J., Park, J.-H., Rey, S.-C., et al., 2003, AJ, 126, 803
Sollima, A., Nipoti, C., 2010, MNRAS, 401, 131
Sollima, A., Bellazzini, M., Lee, J.-W., 2012, ApJ, 755, 156
Villanova, S., Geisler, D., Carraro, G., Moni Bidin, C., Muñoz, C., 2013, ApJ, 778, 186
Walker, M. G. et al., 2006, AJ, 131, 2114
Williams, L.L.R., Barnes, E.I., & Hjorth, J., 2012, MNRAS, 423, 3589
Wilson, C. P., 1975, AJ, 80, 175
Wolf, J., Martinez, G.D., Bullock, J.S., Kaplighat, M., Geha, M., Muñoz, R.R., Simon, J.D., Avedo, F.F., 2010, MNRAS, 406, 1220